Fermi National Accelerator Laboratory

FERMILAB-Pub-75/27-EXP
7100.186

(Submitted to Physical Review)

PROTON-DEUTERON ELASTIC SCATTERING AT SMALL MOMENTUM TRANSFER FROM 50 TO 400 GeV/c

Y. Akimov, L. Golovanov, S. Mukhin, A. Sandacz,
G. Takhtamyshev, and V. Tsarev
Joint Institute for Nuclear Research, Dubna, USSR

E. Malamud, R. Yamada, and P. D. Zimmerman
Fermi National Accelerator Laboratory, Batavia, Illinois 60510 USA

R. Cool, K. Goulianos, and H. Sticker
Rockefeller University, New York, New York 10021 USA

and

D. Gross, A. Melissinos, D. Nitz, and S. Olsen
University of Rochester, Rochester, New York 14627 USA

August 1975

FERMILAB-Pub-75/27-EXP

Rockefeller University
COO-2232A-30

University of Rochester
COO-3065-122 UR-544

PROTON-DEUTERON ELASTIC SCATTERING AT SMALL MOMENTUM TRANSFER FROM 50 TO 400 GeV/c*

Y. Akimov, R. Cool, L. Golovanov, K. Goulianos, D. Gross, E. Malamud, A. Melissinos, S. Mukhin, D. Nitz, S. Olsen,† A. Sandacz, H. Sticker, G. Takhtamyshev, V. Tsarev,‡ R. Yamada, and P. D. Zimmerman§

Fermi National Accelerator Laboratory, Batavia, Illinois 60510
Joint Institute for Nuclear Research, Dubna, USSR
Rockefeller University, New York, New York 10021
University of Rochester, Rochester, New York 14627

August 1975

ABSTRACT

Proton-deuteron elastic scattering has been measured in the four-momentum transfer squared region $0.013 < |t| < 0.14\ (\mathrm{GeV/c})^2$ and for incident proton beam momenta from 50 to 400 GeV/c. The data can be fitted with the Bethe interference formula. We observe shrinkage of the diffraction cone with increasing energy equal to $(0.94 \pm 0.04) \ln(s/1\ \mathrm{GeV}^2)\ (\mathrm{GeV/c})^{-2}$. This shrinkage is greater than that observed in the pp elastic scattering.

The ratio of the elastic to the total cross section is approximately 0.1 and independent of energy above ~150 GeV.

In order to extract information on pn scattering we fit our data using the Glauber approach and a form factor which is the sum of exponentials. The values we obtain for the slope parameter in pn scattering are sensitive to the details of the inelastic double scattering term.

I. INTRODUCTION

In an experiment performed at the Fermi National Accelerator Laboratory we have measured proton-deuteron elastic scattering

$$p + d \rightarrow p + d \qquad (1)$$

at incident proton momenta $50 < p_{lab} < 400$ GeV/c and at values of four-momentum transfer squared in the range $0.013 < |t| < 0.14\ (\text{GeV/c})^2$. From the measurements we have determined the slope of the diffraction cone, b_d, and its energy dependence. Using the Glauber approach we have obtained information on the slope of the diffraction cone for p-n scattering, the deuteron form factor $|S(t)|$, and the energy dependence of the double scattering term.

Previous measurements of pd elastic scattering up to 70 GeV/c incident momentum at Serpukhov[1] showed shrinkage of the deuteron diffraction cone with increasing energy and an analysis of these measurements[2] yielded a parametrization of the deuteron form factor. We have extended these measurements to higher energy using the same basic technique of a gas jet target[3] and the detection of slow recoils by solid state

detectors.[4-9] The jet could be pulsed at any desired time in the acceleration cycle thus allowing data to be taken over a wide range of incident proton momentum.

Diffraction dissociation of the incident proton

$$p + d \rightarrow X + d \qquad (2)$$

was measured simultaneously. The analysis of reactions (1) and (2) are interrelated since reaction (2) forms a background which must be subtracted when studying reaction (1). In addition knowledge of the deuteron form factor obtained in (1) is used to interpret (2) in terms of nucleon-nucleon inelastic scattering. Results on reaction (2) for the same t and incident beam momenta regions over which (1) was measured and for $m_p^2 < M_X^2 < 40\ (GeV/c)^2$ are published elsewhere.[10] Preliminary results on both reactions (1) and (2) have been reported.[11]

In sections II and III we describe the experiment and details of the analysis. Our final elastic data sample consists of 225 measurements at 10 different incident beam momenta. In section IV we discuss the results of fits where the deuteron is considered as a single target particle. The Glauber approach and fits from which we obtain information on proton-neutron scattering and the deuteron form factor are discussed in section V.

II. EXPERIMENTAL PROCEDURE AND APPARATUS

Figure 1 is a schematic layout of the experiment. The circulating beam in the main ring of the Fermilab accelerator intercepted a low density gas jet deuterium target and recoil particles traveled 2.5 meters to the detectors in the "ion guide," a vacuum tank connected directly to the

accelerator vacuum system. The solid state silicon detectors were mounted on a movable carriage so their angle could be changed. The energy and angular resolution were sufficient to isolate the elastically scattered deuterons from background.

The t value was obtained from the kinetic energy, T, of the recoil deuteron measured by total absorption in the silicon detectors:

$$|t| = 2m_d T. \tag{3}$$

For elastic scattering the kinematics are given by

$$|t| = \frac{4m_d^2\beta^2\sin^2\omega}{1 - \beta^2\sin^2\omega}, \tag{4}$$

where m_d is the deuteron mass, $\beta = p_{lab}/(E_{lab} + m_d)$, the center-of-mass velocity, and ω is the recoil angle from 90°. For small angles (near 90° in the laboratory) this becomes

$$|t| \approx 4m_d^2\beta^2\sin^2\omega. \tag{5}$$

The recoil kinematics are almost independent of p_{lab}; thus, this arrangement is ideal for determining the shrinkage of the diffraction cone with increasing energy.

The $|t|$ region studied in this experiment, $0.013 < |t| < 0.14\ (\mathrm{GeV/c})^2$, corresponds to recoil angles of $30 < \omega < 100$ mrad, recoil kinetic energies of $3.5 < T < 37$ MeV, and ranges in silicon of $80 < R < 4000\mu$.

The typical jet operating conditions were density 10^{-7} g/cm^2, jet size at the beam 12 mm, and jet pulse length ~ 200 msec. This density is low enough that multiple scattering of the recoil deuterons was negligible.

Usually the jet was pulsed three times during an acceleration cycle as shown in Fig. 2. The magnetic field in the accelerator was recorded every 20 msec allowing fine binning in the incident beam momentum.

The recoil deuterons were detected by a sandwich of two solid state detectors. The front detectors were 200μ totally depleted surface barrier silicon detectors while the back detectors were either 2000μ surface barrier or 5000μ Li drifted detectors. This choice allowed a measurement of kinetic energies from a threshold of $\lesssim$1 MeV to 42 MeV. Deuterons that penetrate the front detector have at least 6.3 MeV kinetic energy. Thick tantalum collimators were placed in front of each detector stack to define the solid angle. The stacks were spaced 17 mrad apart and mounted on a movable carriage whose angle with respect to the jet could be adjusted from run to run. One stack, however, was held at a fixed angle to monitor the interaction rate.

A schematic diagram of the electronics is shown in Fig. 3. Pulses from detectors were amplified; one of the two amplified outputs was discriminated and served to trigger the peak detecting circuit. Typically, the trigger for a peak detector was either a signal in the front detector or a coincidence between front and back detectors. The electronics for each detector stack operated independently and asynchronously from the others.

When a trigger occurred the analog signal from each detector was gated into a peak detecting circuit. Here the maximum pulse height was retained as an analog voltage and a busy flag was set. A commutator scanned

sequentially through the channels at 5 MHz. When it reached a busy channel it stopped and the analog voltages were routed through a multiplexer into two ADC's which formed eight bit binary numbers which corresponded to the pulse heights in the detectors. These two numbers formed the lower 16 bits of a 24 bit event word which was stored in one of two fast buffer memory units. Four of the remaining bits served to identify the channel. After the event word was stored, the peak detector was reset and the commutator resumed scanning for busy channels.

When one buffer memory was full it was disabled and a PDP 11 computer read it out. In the mean time the other buffer memory unit was enabled and data taking continued without interruption. In addition to writing the data on magnetic tape the computer generated the gates for the experiment and recorded sundry data before and after each gate, for example the beam momentum and intensity. Also while data were being collected the computer monitored the operation of the detectors and the gas jet target.

The data rate in each channel was typically 100 to 150 counts per 200 msec jet burst. Each channel operated independently; an event in a channel caused that channel to be off for typically 10 μsec, while the other channels continued to accept data. The dead time losses in each channel were monitored by scaling all coincidences in each channel including those which occurred during the conversion time for accepted events. These scaled number of triggers were read into the computer at the end of each gate.

The peak detectors were constructed so as to be able to accept pulses with widely varying rise times. This was important because the charge

collection time can differ substantially from detector to detector. For example a 200μ surface barrier detector collects all the deposited charge in less than 200 nsec. On the other hand the 5 mm Li drifted detectors usually require more than 1 μsec to collect all of the deposited ionization.

The linearity of the electronics was checked by sending test pulses of varying pulse heights into the test inputs of the preamps and recording the output pulse heights. Since the test inputs are parallel to the detector inputs these test pulses appear like events to the electronic system. Calibration tapes were written in this way periodically in order to monitor changes in linearity or gain. Fluctuations in electronic performance proved to be minimal. The electronics were linear to ±1 channel and the electronic resolution was likewise within one channel. The electronic contribution to the experimental resolution was entirely negligible.

The energy of the front detectors was calibrated using a $_{96}Cm^{244}$ (5.806 MeV) α-source. The back detectors were calibrated using the elastic peak and the measured angle of the detector stack, which are related through Eq. (4).

III. DATA ANALYSIS

A. Extraction of Elastic Counts

Events detected in a stack can fall into one of three categories: a) particles that stop in the front detector, b) particles that stop in the back detector, and c) particles that cross both detectors. Figure 4 shows a plot of front detector pulse height vs. back detector pulse height in a typical stack. One observes that for events that stop in the back detector deuterons and protons are well separated.

1. Particles That Stop in the Back Detector

The mass of a particle stopping in the back element is given by the empirical formula

$$m = m_p \left\{ \frac{\alpha}{d_F} \left| (T_F + T_B)^{\beta} - T_B^{\beta} \right| \right\}^{\frac{1}{(\beta - 1)}}, \qquad (6)$$

where $\alpha = 0.0133$, $\beta = 1.73$, d_F is the thickness of the front detector in mm, and $T_F(T_B)$ the energy deposited in the front (back) detector in MeV.

Figure 5 shows a plot of m/m_p for all events in a stack. The proton and deuteron peaks are well separated. The resolution in the mass of the recoil particle is primarily due to the relative precision of the dT/dx measurement. This could be improved, at the expense of increasing the minimum kinetic energy of recoils of type b, by increasing the thickness of the front detector. The 200μ front detectors represented a compromise which yielded adequate mass resolution with a relatively small threshold for counting in the rear detector (T = 7 MeV). The events in Fig. 5 with very low masses are due to particles from category (c). Deuterons were defined by the following cuts: $1.5 < m/m_p < 2.5$ and $0.03 < |t| < 0.075$ $(GeV/c)^2$ for the 2000μ detectors or $0.03 < |t| < 0.15$ $(GeV/c)^2$ for 5000μ detectors. The lower cut on $|t|$ was to insure that the deuteron has recorded a back detector energy sufficiently above threshold. The higher $|t|$ cut avoided the region where a two-fold ambiguity exists as to whether the particle has penetrated the rear detector or not.

Figure 6 shows the kinetic energy distribution of deuterons at two different incident momenta. The peak is the elastic peak. Events at lower

kinetic energy are due to reaction (2). The width of the elastic peak reflects the angular resolution of the apparatus. From Eq. (5) we find

$$2m_d\Delta T = \Delta|t| \simeq 8m_d^2\beta^2\omega\Delta\omega, \tag{7}$$

where $\Delta\omega \simeq 3$ mrad (HWHM) reflecting the 12 mm width of the jet and the 5 mm effective width of the detectors. Elastic events were counted within ± 3 standard deviations of t_{el}, where t_{el} was determined from the angle of the stack [Eq. (4)]. Since our cuts defining a deuteron demand that $|t|_{el} - 3\sigma$ be greater than 0.03 $(GeV/c)^2$ and $|t|_{el} + 3\sigma$ be less than 0.075 $(GeV/c)^2$ (for a 2000μ detector) or less than 0.15 $(GeV/c)^2$ (for a 5000μ detector) we further required that

$$0.035 < |t_{el}| < 0.07\ (GeV/c)^2$$

or

$$0.035 < |t_{el}| < 0.14\ (GeV/c)^2.$$

The fixed detector was treated in the same way as all other detectors. The number of elastic events in each detector, ΔN, in solid angle $\Delta\Omega$, were converted to $d\sigma/dt$ as follows:

$$\frac{d\sigma}{dt} = \frac{\Delta N}{\Delta\Omega}\,\frac{\pi}{2m_d\sqrt{|t|}}\left(\frac{d\sigma}{d\Omega}\right)_{fixed}\Bigg/\left(\frac{\Delta N}{\Delta\Omega}\right)_{fixed}, \tag{8}$$

where $(d\sigma/d\Omega)_{fixed}$ and $(\Delta N/\Delta\Omega)_{fixed}$ are for the fixed monitor. The correct normalization was obtained in the final fits from the optical theorem and proton-deuteron total cross sections.

2. Particles That Stop in the Front Detector

For particles that stopped in the front detector no mass separation of deuterons can be made. Consequently the analysis proceeded in a fashion similar to that described in Refs. 1, 6, and 7 where only one detector was used to observe the elastic peaks. The peak sits on top of a background of protons and minimum ionizing particles. We used the back detector to remove fast particles leaving mostly low energy protons and deuterons and significantly reducing the background under the peak. Moreover, we treated the front and back detector together as a single detector (for deuterons) up to $|t|_{el} = 0.035\ (GeV/c)^2$ for cases where the elastic peak was contained partially in the front detector and partially in the back. Thus no gap in the $|t|$ distribution appears and no biases are introduced because of partially observed peaks.

To measure the remaining proton background under the peak we assumed that it is angle independent over a small angular range and measured the front detector distribution at recoil angles closer to 90° (or even beyond 90°). Since we normalized to a fixed detector, we could test the assumption by comparing the cross section away from the elastic peak with the background cross section. In all cases the agreement was better than 10% in the $|t|$ regions where we made the subtraction. Consequently we assigned 10% uncertainty to the subtraction. Since the subtraction did not exceed 10% the additional uncertainty was typically smaller than 1%.

3. Particles That Penetrate Both Detectors

In this case one could treat front and back detectors as a single detector. Together they measure the dE/dX of a penetrating particle, which, for elastic events, still shows a peak. However, this peak has significant background contributions from inelastic events and minimum ionizing particles that cannot easily be measured or subtracted without introducing large uncertainties. Consequently, we chose to discard these data.

B. Inelastic Subtraction

At low momentum (i.e., 50 GeV/c), the elastic peak is well separated from the threshold for single π production. At higher energies this threshold moves to well within the elastic peak, requiring that the inelastic events be subtracted from the elastic events. To perform this subtraction we parametrized the inelastic cross sections[10,11] with the formula

$$\frac{d^2\sigma}{dtdM_x^2} = A\left(1 + \frac{B}{p_{lab}}\right)\frac{1}{M_x^2}\left[1 - e^{\beta(M_x^2)}\right]b_x(M_x^2)e^{b_x t}F_d(t) \qquad (9)$$

for $M_x \geq m_p + m_\pi$ and where A = 0.54 mb, B = 54 GeV/c, $\beta(M_x^2)$ $= [M_x - (m_p + m_{\pi^o})]^2/2m_\pi^2$, and the slope b_x is given by:

$$b_x(M_x^2) = 5.5\left[1.0 + \frac{0.06}{(M_x - 1.36)^2 + 0.02}\right]. \qquad (10)$$

F_d, the "coherence factor," $= 3.6e^{25.9|t| + 60|t|^2}$. The factor 3.6 is approximately the square of ratio of the measured pd and pp total cross sections in our energy range.[12,13] This formula reproduces the behavior of the inelastic cross section quite well, including the large peak at $M_x \approx 1400$ MeV with

its steep t dependence, the $(1/M_x^2)$ behavior at large masses, and the threshold cutoff at the $m_p + m_\pi$ threshold. This cross section, transformed to a fixed angle cross section and integrated within the elastic $|t|$ cuts, was subtracted from the normalized elastic cross section. This was an iterative procedure since the inelastic measurements required knowledge of the elastic cross section for normalization.

We assign a conservative 10% uncertainty to this subtraction.

C. Systematic Errors

1. Angle

The absolute angle of the carriage was determined from the energy of elastic peaks wholly contained in the front detector, for which accurate calibrations exist. The resultant angular uncertainty, due to uncertainty in the peak channel, is ±0.2 mrad.

2. Area

The area subtended by each detector was determined by a tantalum collimator. The relative areas of these collimators were measured with a thick $_{95}Am^{241}$ (5.486 MeV) α-source. The uncertainty in area is ±0.5%.

3. Dead Time

Dead time losses were monitored in each channel. Losses were always $\lesssim$ 2% and varied from channel to channel by $\lesssim$ 0.5%.

4. Nuclear Interactions in the Detectors

We assume that d-silicon interactions ($\simeq$ 1 barn) are mostly stripping reactions. These are energy independent so the probability of a nuclear interaction is proportional to the range. When geometrical factors in our setup are included we obtain

$$\left.\frac{d\sigma}{dt}\right|_{\text{corrected}} = \left.\frac{d\sigma}{dt}\right|_{\text{measured}} \left(1 + 0.46|t|^{1.73}\right), \tag{11}$$

where t is in $(\text{GeV}/c)^2$. Thus the maximum correction at $|t| = 0.137\ (\text{GeV}/c)^2$ is 1.5%. We assign 15% uncertainty to this correction.

Some of these corrections are p_{lab} and/or t dependent. In Table I we summarize the various contributions to the error for data points at the extremes of our p_{lab} and t regions. Figure 7 shows the differential cross section at two values of incident momentum.

IV. pd ELASTIC SCATTERING RESULTS

The Bethe interference formula[14] was used to include the small ($\lesssim 2\%$ in our t-range) electromagnetic effects. This well known formula can be written as:

$$\frac{d\sigma}{dt} = \left\{ f_I^2(t)\,(1+\rho^2) + f_c^2(t) + 2f_c(t)\,f_I(t)\left[\rho + 2n \ln \frac{1.06\hbar}{R\sqrt{|t|}}\right]\right\}, \tag{12}$$

where $n = [(1/137.04)(1/\beta_{lab})]$, ρ is the ratio of the real to the imaginary parts of the forward scattering amplitude, β_{lab} is the incident proton velocity, and R is the radius of the strong interaction region. In our energy region there are no measurements of ρ for proton-deuteron scattering. At lower energies ρ_{pd} is approximately equal to ρ_{pp}.[15] Therefore, in all of the pd fits we set $\rho(s_{pp}) = -0.61 + 0.10 \ln s_{pp}$, where s_{pp} is defined as the center-of-mass energy squared in the nucleon-nucleon system expressed in units of 1 GeV^2. This is a good approximation to measurements of $\rho(s_{pp})$ in pp

scattering in our energy range.[7] In Eq. (12) the spin-flip amplitude is neglected.

In applying Eq. (12) to pd scattering we use[17] $R = 2.7\sqrt{10}$ mb$^{\frac{1}{2}}$. The Coulomb amplitude is written as

$$f_c = \frac{2n\hbar\sqrt{\pi}}{t} G_p G_d, \tag{13}$$

where

$$G_p = \frac{1}{\left(1 - \frac{t}{0.71}\right)^2}, \tag{14'}$$

and

$$G_d = e^{\frac{(25.9t + 60t^2)}{2}}. \tag{14''}$$

The exact form used for the electromagnetic form factors is not of consequence since these terms make a small contribution in our t-range.

In small angle pd scattering, in contrast to pp scattering, $(d\sigma/dt)$ cannot be well described by a simple exponential. Instead a more complex t-dependence is needed to describe the observed "curvature" in the differential cross section.

Bartenev et al.[1] modified the t-dependence of the nuclear amplitude to include a quadratic term:

$$f_I = \frac{\sigma_{tot}}{4\sqrt{\pi}\,\hbar} e^{\frac{(bt + ct^2)}{2}} \tag{15}$$

We used Eqs. (12), (13), and (15) to fit[16] the data. We parametrized b as $b_0 + b_1 \ln s_{pd}$ where s_{pd} is the center-of-mass energy squared in the pd system; b_1 measures the shrinkage of the diffraction cone. We obtained $\chi^2 = 414$ for 225 data points and 13 parameters: 10 normalization constants,

one for each energy, b_0, b_1, and c. The values obtained were $b_0 = 32.8 \pm 0.6$ $(GeV/c)^{-2}$, $b_1 = 1.01 \pm 0.09$ $(GeV/c)^{-2}$ and $c = 54.0 \pm 0.9$ $(GeV/c)^{-4}$. The errors in this and subsequent fits do not include a scale factor from the χ^2.

A somewhat better fit can be obtained using a different empirical t-dependence for f_I. Anticipating the results discussed in Section V, we write:

$$f_I = \frac{\sigma_{tot}}{4\sqrt{\pi}\,\hbar}\left[0.34e^{\left(\frac{141.5t}{4}\right)} + 0.58e^{\left(\frac{26.1t}{4}\right)} + 0.08e^{\left(\frac{15.5t}{4}\right)}\right] \times e^{(b_0 + b_1 \ln s_{pp})\frac{t}{2}} \qquad (16)$$

The choice of these particular constants is described in the next section. We also note that Eq. (16) avoids the awkward divergence as $|t| \to \infty$ present in Eq. (15).

We fit the 225 data points to Eqs. (12), (13), and (16) with 12 parameters: 10 normalization constants, one for each energy, and the parameters b_0 and b_1. We obtained $\chi^2 = 274$, $b_0 = 8.46 \pm 0.26$ $(GeV/c)^{-2}$ and $b_1 = 0.94 \pm 0.04$ $(GeV/c)^{-2}$. We conclude that Eq. (16) is a better description of the data than Eq. (15). The shrinkage agrees with that obtained using the quadratic form for the amplitude. However, the value is larger than $b_1 = 0.556 \pm 0.028$ $(GeV/c)^{-2}$ measured in pp scattering.[7]

We can also use Eqs. (12), (13), and (15) to fit each energy independently. The form (15) is used in order to compare with the lower energy experiment.[1] Values of b and c from these energy independent fits are summarized in Table II and plotted in Fig. 8. We estimate that s-independent errors such as angle calibration could result in an overall systematic shift of ± 0.2 $(GeV/c)^{-2}$ in the b-values shown.

In Table III are listed values of $d\sigma/dt$ for our 225 data points. Since with the gas jet technique we do not obtain absolute cross sections we have normalized our data using the optical theorem and the following expression for the total pd cross section:

$$\sigma_{tot}\,pd(mb) = 99.73 - 9.40 \ln s_{pd} + 0.829 \ln^2 s_{pd}. \qquad (17)$$

This expression is a good empirical fit to the published pd cross sections of Gorin et al.[12] and Carroll et al.[13] The normalization of the data in Table III was obtained using Eq. (15) for f_I.

In order to obtain the elastic pd cross section we integrated the nuclear part of the differential cross section over t. This was done using parameters obtained at each energy by fitting our data to Eqs. (12), (13), and (16).

The integration was carried out to $|t| = \infty$. Values of $|t| > 0.14 (GeV/c)^2$, beyond our measured range, contribute ~1.4% to the elastic cross section. An estimate of the high t tail using the Glauber approach and including d-wave effects and the possible inelastic contributions to the double scattering term gives a result similar to that obtained using Eqs. (12), (13), and (16). But this high t contribution may be uncertain by as much as a factor of two. This uncertainty as well as the systematic uncertainty in σ_{tot}[13] produce a systematic uncertainty in the ratio σ_{el}/σ_{tot} of about ±0.002. There is a large contribution to σ_{el} from t values below our region of measurement [$|t| < 0.013\ (GeV/c)^2$]. Consequently the integrated cross section is sensitive to the parametrization of the differential cross section.

Values of σ_{el} and σ_{el}/σ_{tot} are given in Table IV and plotted in Fig. 9, together with lower energy data.[17,18] The errors shown in the table and on the figure for our data do not include the overall energy independent uncertainty. The values from Refs. 17 and 18 were calculated using $e^{bt + ct^2}$ and integrating from $0 \leq |t| \leq 0.2\ (GeV/c)^2$ and corrected for the high t contribution. Our points are calculated using Eq. (16) and integrating from $0 \leq |t| \leq \infty$. The dashed curve shows how σ_{el}/σ_{tot} for our experiment changes if we use e^{bt+ct^2} and integrate from $0 \leq |t| \leq 0.14\ (GeV/c)^2$ and adding 1.4% for the contribution from high-t.

The ratio of σ_{el}/σ_{tot} is constant for $p_{lab} \geq 150$ GeV/c supporting the existence of a Van Hove limit and the geometrical scaling hypothesis.[19] This constancy of σ_{el}/σ_{tot} for $p_{lab} \geq 100$ GeV/c has also been observed in pp scattering.[20] The smaller value of σ_{el}/σ_{tot} for pd scattering can be interpreted as a greater transparency to the scattering disk.

V. THE GLAUBER APPROACH AND PROTON-NEUTRON SCATTERING

In the Glauber approach[21-24] elastic pd scattering is described as a coherent sum of Coulomb, single nucleon, and double nucleon scattering. Assuming s-wave scattering and only elastic rescattering (these assumptions will be discussed below) we can write:

$$\frac{d\sigma}{dt} = \left| S\left(\frac{t}{4}\right) [A_C + A_p + A_n] + A_G \right|^2 , \tag{18}$$

where

$$A_C = \frac{2}{137.04} \frac{1}{\beta_{lab}} \frac{\hbar\sqrt{\pi}}{t} e^{b_{pp}\frac{t}{2}} e^{i\eta} .$$

$$A_p = e^{i\chi_{cp}} \frac{\sigma_{pp}}{4\sqrt{\pi}\hbar}(i + \rho_{pp}) e^{b_{pp}\frac{t}{2}}$$

$$A_n = e^{i\chi_{cn}} \frac{\sigma_{pn}}{4\sqrt{\pi}\hbar}(i + \rho_{pn}) e^{b_{pn}\frac{t}{2}}$$

$$A_G = e^{i\chi_{cpn}} \frac{i\hbar}{\sqrt{\pi}} \frac{\sigma_{pp}\sigma_{pn}}{(4\sqrt{\pi}\hbar)^2}(i + \rho_{pp})(i + \rho_{pn}) \times e^{\frac{t(b_{pp}+b_{pn})}{8}} \text{IG}.$$

S(t) is the deuteron form factor, β_{lab} is the incident proton velocity in the laboratory, b_{pp}, b_{pn}, ρ_{pp}, ρ_{pn}, σ_{pp}, σ_{pn} are the slope parameters, real to imaginary forward nuclear scattering amplitude ratios, and total cross sections for pp and pn scattering respectively, and η, χ_{cp}, χ_{cn}, and χ_{cpn} are phases between the amplitudes. IG is the Glauber integral defined as

$$\text{IG} = \tfrac{1}{2} \int_{-\infty}^{0} S(t)\, e^{b_{pp}\frac{t}{2}} e^{b_{pn}\frac{t}{2}}\, dt. \tag{19}$$

We calculate phases using the formulas in Ref. 24: $\chi_{cp} = 0.10$, $\chi_{cn} = 0.11$, $\chi_{cpn} = 0.10$, $\eta = (2/137.03)[\ln(2p_{lab}/\sqrt{|t|}) - 0.577]$.

In our incident momentum and t range, η varies from 0.08 to 0.12. The phases used in the earlier analyses[2,25] differ from ours due to a different approach in calculating them but the effect of changing these phases in our t-range is small.

For the pp total cross section we use the following empirical formula describing measured data:[12,13]

$$\sigma_{tot_{pp}}(\text{mb}) = 50.866 - 5.2303 \ln s_{pp} + 0.5437 \ln^2 s_{pp}. \tag{20}$$

For ρ_{pp} we use measured values.[7] For b_{pp} we use the published fit to measured values:[6]

$$b_{pp} = 8.23 + 0.556 \ln s_{pp}. \tag{21}$$

s_{pp} is measured in units of 1 GeV^2.

In the following fits we have assumed $\rho_{pn} = \rho_{pp}$[26] and $\sigma_{pn} = \sigma_{pp}$.[27] Zolin et al.[2] using data below 27 GeV/c have fit data to the following form factor:

$$S\left(\frac{t}{4}\right) = e^{\frac{(bt + ct^2)}{2}}. \tag{22}$$

We have applied this form factor to our data. If we assume $b_{pn} = b_{pp}$ we obtain $b = 26.5 \pm 0.1\ (GeV/c)^{-2}$ and $c = 62.7 \pm 0.8\ (GeV/c)^{-4}$. This is in good agreement with Zolin et al.[2] who obtained $b = 25.9 \pm 1.2\ (GeV/c)^{-2}$ and $c = 60 \pm 5\ (GeV/c)^{-4}$. Our fit has $\chi^2 = 495$ for 213 degrees of freedom. If b_{pn} is allowed to vary in the fit and b and c are fixed at the values of Ref. 2, the χ^2 is only slightly improved.

We note that Zolin et al.[2] used np, pp, and pd scattering data to obtain their form factor, whereas ours is determined only from pd data with the assumption that the pn and pp scattering amplitudes are equal.

An improved fit is obtained by using a form factor which is a sum of exponentials:[24]

$$S\left(\frac{t}{4}\right) = A_1 e^{\frac{B_1 t}{4}} + A_2 e^{\frac{B_2 t}{4}} + (1 - A_1 - A_2) e^{\frac{B_3 t}{4}}. \tag{23}$$

In Table V are presented the results of fits using Eq. (23) both with fixed values for A_i and B_i obtained from Ref. 24 and also allowing A_i and B_i to vary.[28] These fits are done both with $b_{pn} = b_{pp}$ and b_{pn} allowed to vary

and have an improved χ^2 over the fit with the quadratic form factor (22). We note that the errors in Table V do not include the error in b_{pp}.

This straightforward application of the Glauber formula results in a neutron shrinkage that is significantly larger than the shrinkage of the proton. Before one can conclude, however, that the behavior of the neutron is different from the proton we must examine possible contributions that have not been included in Eq. (18) which may give such an effect. These contributions include a t dependent real-to-imaginary ratio, deuteron d wave, and inelastic double scattering. If our data were absolutely normalized we could subtract Eq. (18) and directly measure these other contributions. We consider the effects of these other contributions on the extracted values of b_0 and b_1.

If we remove the implicit assumption in (18) that the ratio of real to imaginary parts of the scattering amplitude is independent of t we can produce a large shift in the values of b_0 and b_1. But no experimental information exists on this point so we assume the t-independence of ρ. To include both s- and d-wave contributions would require us to fit[29] our data to the following equation:

$$\begin{aligned}\frac{d\sigma}{dt} &= \left|S_0\left(\frac{t}{4}\right)[A_c + A_p + A_n] + A_{G_s}\right|^2 \\ &+ \frac{1}{4}\left|S_2\left(\frac{t}{4}\right)[A_p + A_n] + A_{G_d}\right|^2 \\ &+ \frac{3}{4}\left|S_2\left(\frac{t}{4}\right)[A_p + A_n]\right|^2.\end{aligned} \tag{24}$$

In Eq. (24) S_0 and S_2 are the spherical and quadrupole deuteron form factors. A_{G_s} and A_{G_d} are the corresponding double scattering amplitudes. The second and third terms become relatively more important as t increases. For example at $|t| = 0.01$ (GeV/c)^2 these terms contribute 0.03% to the cross section and at $|t| = 0.10$ (GeV/c)^2 they contribute 4% to the cross section. At larger t-values A_c is negligible and is therefore not included in these terms.

To apply Eq. (24) to our data requires us to input information on the form factors from other work.[30] We have done some fits using this approach and find that at each energy b_{pn}, the parameter of most interest to us, is changed by $\lesssim 10\%$ and the shrinkage is not appreciably changed. Therefore, we choose in what follows to neglect the d-wave contribution.

Another complication is that the double scattering term in Eqs. (18) and (19) may contain contributions from inelastic intermediate states. This contribution has an unknown energy and t dependence. In an attempt to calculate these contributions we have fitted our data to Eq. (18) with $b_{pn} = b_{pp}$, $G(t)$ from Ref. 24, and with IG as a free parameter at each energy.

The results plotted in Fig. 10 show a slight increase with incident momentum but the statistical significance of this rise is weak. Between 50 and 200 GeV/c the Fermilab total cross section experiment[32] does not measure an increase in IG obtained from πd total cross section measurements. In analyzing their pp and pd total cross section data[13] they use the value 0.035 ± 0.004 mb^{-1}. On the other hand, a recent analysis[33] of the total cross section data predicts a rise in the shadow correction.

It is not expected that the inelastic and elastic contributions to A_G have the same t-dependence. This problem was considered by Kwieciński et al.[31] for πd scattering. They calculate an inelastic contribution rising with energy and with a t dependence steeper than the t dependence of elastic double scattering. The rise with energy they calculate is consistent with the value of IG measured at Serpukhov but not consistent with more recent total cross section measurements at Fermilab,[32] which give an energy independent value of 0.039 ± 0.001 mb^{-1}. We follow the approach of Ref. 31 and modify A_G as follows:

$$A_G = A_{G_{el}} + A_{G_{inel}}, \tag{25}$$

where $A_{G_{el}}$ is given by Eqs. (18) and (19) and

$$A_{G_{inel}} = i(0.1 - 0.064 \ln p_{lab})e^{9t} \tag{26}$$

For comparison

$$A_{G_{el}} = -i(0.74)e^{2.8t}. \tag{27}$$

We use our inelastic data[10] to evaluate Eq. (26) by assuming that the triple Pomeron coupling accounts for about 60% of the inelastic cross section and has a t-dependence of e^{6t}. With this input we can now perform a fit with the following 12 parameters: 10 normalization constants, and b_0, b_1 which give the neutron slope parameter as a function of energy. The results are $\chi/DF = 267/213$, $b_0 = 6.3\pm0.5$ (GeV/c)$^{-2}$, $b_1 = 0.92\pm0.09$ (GeV/c)$^{-2}$.

There is an estimated 100% uncertainty in the inelastic shadow correction given by Eq. (26). The value of b_1 is very sensitive to this correction.

If the error in Eq. (26) is folded in b_1 can vary from 0.7 to 1.15. The former value for neutron shrinkage is comparable to the proton shrinkage. The latter value is that found with no inelastic correction and shown in Table V.

VI. CONCLUSIONS

Proton-deuteron elastic scattering has been measured using the circulating beam in the Fermilab accelerator intercepting a thin gas jet target. The recoil deuteron was detected with stacks of solid state detectors. The t and incident beam momentum ranges covered were $0.013 < |t| < 0.14\ (\mathrm{GeV/c})^2$ and $50 < p_{lab} < 400$ GeV/c.

From these measurements we have fitted the differential cross section and observed shrinkage of the nuclear diffraction cone with increasing energy. We find this shrinkage equal to $(0.94\pm0.04)\ \ln(s/1\ \mathrm{GeV}^2)(\mathrm{GeV/c})^{-2}$ which is greater than that observed in pp elastic scattering. The data are fit better by a form which is the sum of three exponentials rather than a single exponential with a quadratic term.

The differential cross section was integrated to obtain the total elastic cross section and the ratio of elastic to total cross section. This ratio is independent of energy above ~150 GeV. Its value, a measurement of target "transparency," is ~0.1, less than for a proton.

We also have attempted to extract information on pn scattering using the Glauber approach. This approach is complicated by spin effects, inelastic contributions to the shadow contribution, and the uncertainty about the t-dependence of the real part of the nucleon-nucleon scattering amplitude. Depending on what is assumed for these contributions, it is possible to show approximate equality of shrinkage in pn and pp elastic scattering.

ACKNOWLEDGMENTS

We acknowledge the support of the operating staff of the Fermi National Accelerator Laboratory whose contributions were essential to the success of this work. The Dubna members of this collaboration wish to acknowledge the support and hospitality of Fermilab during their stay.

REFERENCES

*This work was supported in part by the U. S. Energy Research and Development Administration under contracts AT(11-1)-2232 and AT(11-1)-3065, and the USSR State Committee for Atomic Energy.

†A. P. Sloan Fellow.

‡Present address: P. N. Lebedev Physical Institute, Moscow, USSR.

§Present address: Department of Physics and Astronomy, Louisiana State University, Baton Rouge, Louisiana 70803.

[1]V. D. Bartenev et al., Sov. J. Nucl. Phys. 15, 650 (1972). [Yad. Fiz. 15, 1174 (1972).]; G. G. Beznogikh, Nucl. Phys. B54, 97 (1973).

[2]L. S. Zolin et al., Sov. J. Nucl. Phys. 18, 30 (1974). [Yad. Fiz. 18, 55 (1973)].

[3]V. D. Bartenev et al., Adv. Cryogenic Eng. 18, 460 (1973).

[4]Y. Akimov et al., JETP (USSR) 21, 507 (1965) and Sov. J. Nucl. Phys. 4, 88 (1966).

[5]V. D. Bartenev et al., Phys. Rev. Lett. 29, 1755 (1972).

[6]V. Bartenev et al., Phys. Rev. Lett. 31, 1088 (1973).

[7]V. Bartenev et al., Phys. Rev. Lett. 31, 1367 (1973).

[8]D. Gross, Low Momentum Transfer Proton-Proton Elastic Scattering up to 400 GeV, Ph.D. Thesis, University of Rochester report UR-503, 1974 (unpublished).

[9]V. Bartenev et al., Phys. Lett. 51B, 299 (1974).

[10] Y. Akimov et al., Excitation of High Energy Protons into Low Mass States in p-d Interactions, submitted to Phys. Rev. Lett.; Y. Akimov et al., Diffraction Dissociation of High Energy Protons in p-d Interactions, submitted to Phys. Rev. Lett.

[11] Papers submitted to XVII International Conference on High Energy Physics, London, July 1-10, 1974, and Fermilab reports (unpublished):
Y. Akimov et al., Proton-Deuteron Elastic Scattering and Diffraction Dissociation from 50-400 GeV, Fermilab Conf-74/56-EXP;
Y. Akimov et al., Excitation of the Proton to Low Mass States at 180 and 270 GeV, Fermilab Conf-74/66-EXP;
Y. Akimov et al., An Analysis of Proton-Deuteron Interactions at Fermilab Energies, Fermilab-Conf-74/79-THY/EXP.

[12] Yu. P. Gorin et al., Sov. J. Nucl. Phys. 17, 157 (1973).

[13] A. S. Carroll et al., Phys. Rev. Lett. 33, 928 (1974).

[14] H. Bethe, Ann. Phys. (N.Y.) 3, 190 (1958).

[15] V. A. Nikitin, Problems of Elementary Particle and Atomic Nucleus Physics 1, 1 (1970).

[16] Fits described in this paper were done with the programs MINUIT (CERN) and FUMILI (JINR-Dubna). Both programs gave similar results.

[17] M. Shafranova, Sov. J. Part. Nucl. 5, 259 (1975).

[18] G. G. Beznogikh, Phys. Lett. 43B, 85 (1973).

[19] J. Dias de Deus, Nucl. Phys. B59, 231 (1973); A. J. Buras and J. Dias de Deus, Nucl. Phys. B71, 481 (1974); L. Van Hove, Rev. Mod. Phys. 36, 655 (1964).

[20] V. Bartenev et al., The Total Elastic Proton-Proton Cross Section from 9 to 300 GeV/c, Dubna preprint E1-8456 (1974).

[21] R. J. Glauber, Phys. Rev. 100, 242 (1955).

[22] V. Franco and R. J. Glauber, Phys. Rev. 142, 1195 (1966).

[23] V. Franco and E. Coleman, Phys. Rev. Lett. 17, 827 (1966).

[24] V. Franco and G. K. Varma, Phys. Rev. Lett. 33, 44 (1974); V. Franco and G. K. Varma, Coulomb Effects in Hadron-Nucleus and Nucleus-Nucleus Collisions and the Hadron-Neutron Amplitude, to be published.

[25] G. G. Beznogikh et al., Sov. J. Nucl. Phys. 18, 179 (1974). [Yad. Fiz. 18, 348 (1973)].

[26] ρ_{pn} has not yet been measured above 70 GeV. Below 70 GeV the authors of Ref. 25 claim experimentally that $\rho_{pn} = \rho_{pp}$ whereas in Ref. 24 the data of Ref. 25 is reanalyzed with another form factor and found to disagree. In this paper we assume $\rho_{pn} = \rho_{pp}$ but clearly more experimental investigation of this assumption is needed.

[27] M. J. Longo et al., Phys. Rev. Lett. 33, 725 (1974).

[28] G. K. Varma, private communication: The form factor given in Ref. 21 agrees with three theoretical form factors (Ried, Bressel-Kerman, and Humbertson, see Ref. 21 for references) to $\lesssim 2.4\%$ for $|t| \leq 0.12\ (\mathrm{GeV/c})^2$. A change in the constants in the Franco-Varma form factor is reasonable if it changes the form factor by $\lesssim 1.5\%$. We have applied this constraint in those fits where we allow the constants in the form factor to vary. We are grateful to G. K. Varma for his assistance on this problem.

[29] D. R. Harrington, Phys. Rev. Lett. 21, 1496 (1968).

[30]G. Alberi, L. Bertocchi, and G. Białkowski, Nucl. Phys. B17, 621 (1970).

[31]J. Kwieciński, L. Leśniak, and K. Zalewski, Nucl. Phys. B78, 251 (1974).

[32]A. S. Carroll et al., Phys. Rev. Lett. 33, 932 (1974).

[33]R. E. Hendrick et al., Phys. Rev. D11, 536 (1975).

Table I. Summary of Errors.

p_{lab} (GeV/c)	49	49	384	384
$\|t\|$ GeV/c)^2	0.013	0.128	0.014	0.137
$d\sigma/dt$ (mb)	187.5	5.13	178.6	3.30
Errors	%	%	%	%
Statistical	0.7	1.2	0.5	1.1
Systematic:				
Angle	0.6	1.3	0.7	1.2
Area	0.5	0.5	0.5	0.5
Dead time	0.5	0.5	0.5	0.5
Background Subtraction	0.6	0.1	0.6	0.7
Nuclear Interactions	0.0	0.1	0.0	0.1
Total Systematic	1.2	1.5	1.2	1.6
Total	1.4	1.9	1.3	2.0

Table II. Fits to Bethe Interference Formula.

p_{lab} GeV/c	Data Points	b (GeV/c)$^{-2}$	c (GeV/c)$^{-4}$	χ^2
49	31	37.7 ± 0.3	51.4 ± 2.5	47.2
72	26	38.3 ± 0.3	51.8 ± 2.4	29.1
148	40	38.3 ± 0.3	47.7 ± 2.0	53.5
174	9	40.6 ± 1.1	67.0 ± 10.1	14.5
221	24	40.7 ± 0.4	62.9 ± 2.8	41.1
248	19	39.4 ± 0.4	53.8 ± 3.0	65.1
270	19	40.2 ± 0.4	55.1 ± 2.9	22.9
289	9	41.0 ± 1.1	65.2 ± 10.1	14.4
346	24	41.1 ± 0.4	62.6 ± 2.8	48.6
384	24	40.7 ± 0.4	57.3 ± 2.7	30.4

Table III. Differential pd Elastic Cross Sections.

p_{lab} GeV/c	-t $(GeV/c)^2$	$d\sigma/dt$ $mb/(GeV/c)^2$	$\Delta(d\sigma/dt)$ $mb/(GeV/c)^2$	p_{lab} GeV/c	-t $(GeV/c)^2$	$d\sigma/dt$ $mb/(GeV/c)^2$	$\Delta(d\sigma/dt)$ $mb/(GeV/c)^2$
49	0.013	189.28	2.58	72	0.012	195.98	2.25
	0.013	179.81	2.32		0.015	176.07	2.02
	0.014	179.00	2.28		0.018	155.97	1.81
	0.016	161.35	2.02		0.021	137.62	1.90
	0.017	158.79	2.03		0.021	136.80	1.69
	0.020	142.07	1.79		0.024	122.77	1.56
	0.020	138.66	1.72		0.024	122.23	1.64
	0.023	122.05	1.62		0.027	108.17	1.34
	0.027	105.24	1.37		0.027	109.61	1.40
	0.032	90.37	1.26		0.031	95.26	1.20
	0.044	60.42	0.83		0.035	83.31	1.10
	0.044	60.48	0.85		0.039	73.06	0.99
	0.053	46.09	0.71		0.043	61.97	0.89
	0.059	37.76	0.59		0.043	62.45	0.99
	0.059	37.58	0.60		0.048	53.81	0.75
	0.059	36.73	0.57		0.048	54.05	0.79
	0.065	30.99	0.50		0.048	54.08	0.84
	0.066	30.01	0.48		0.048	52.61	0.76
	0.068	27.63	0.42		0.053	46.21	0.67
	0.078	21.25	0.35		0.053	45.28	0.68
	0.080	20.46	0.35		0.058	39.36	0.58
	0.084	17.92	0.30		0.063	33.25	0.50
	0.087	16.09	0.28		0.068	27.97	0.43
	0.090	14.86	0.26		0.121	6.40	0.12
	0.095	13.19	0.23		0.128	5.23	0.09
	0.096	12.79	0.24		0.136	4.11	0.08
	0.103	10.55	0.19				
	0.111	8.27	0.16				
	0.119	6.61	0.12				
	0.128	5.35	0.11				
	0.128	5.18	0.10				

Table III. Differential pd Elastic Cross Sections.

p_{lab} GeV/c	-t $(GeV/c)^2$	$d\sigma/dt$ mb/$(GeV/c)^2$	$\Delta(d\sigma/dt$ mb/$(GeV/c)^2$	p_{lab} GeV/c	-t $(GeV/c)^2$	$d\sigma/dt$ mb/$(GeV/c)^2$	$\Delta(d\sigma/dt)$ mb/$(GeV/c)^2$
148	0.014	178.27	2.14	148	0.067	27.07	0.42
	0.014	169.94	2.31		0.068	25.46	0.43
	0.017	157.40	1.84		0.084	16.53	0.30
	0.017	153.25	1.99		0.092	13.09	0.24
	0.018	144.22	3.32		0.099	10.48	0.19
	0.020	137.49	1.72		0.102	9.65	0.36
	0.021	133.88	1.81		0.108	8.31	0.17
	0.023	121.29	1.50		0.116	6.21	0.13
	0.024	112.57	1.54		0.125	5.00	0.10
	0.028	102.70	1.30		0.126	5.03	0.09
	0.029	98.63	1.36		0.134	3.91	0.07
	0.029	99.03	1.25		0.135	3.76	0.09
	0.032	86.53	1.13		0.135	3.80	0.08
	0.033	83.85	1.09				
	0.033	82.39	1.22				
	0.038	71.89	0.96				
	0.042	60.73	0.88				
	0.047	51.47	0.74				
	0.049	49.31	0.70	174	0.013	204.93	2.84
	0.054	42.15	0.62		0.015	179.32	2.23
	0.056	39.55	0.65		0.018	156.78	2.00
	0.056	39.54	0.58		0.021	139.01	1.70
	0.060	34.21	0.52		0.070	26.62	0.43
	0.061	33.19	0.50		0.082	18.18	0.30
	0.062	30.95	0.51		0.089	15.14	0.25
	0.062	32.96	0.54		0.095	12.47	0.22
	0.062	32.61	0.52		0.102	10.28	0.19

Table III. Differential pd Elastic Cross Sections.

p_{lab} GeV/c	-t $(GeV/c)^2$	$d\sigma/dt$ $mb/(GeV/c)^2$	$\Delta(d\sigma/dt)$ $mb/(GeV/c)^2$	p_{lab} GeV/c	-t $(GeV/c)^2$	$d\sigma/dt$ $mb/(GeV/c)^2$	$\Delta(d\sigma/dt)$ $mb/(GeV/c)^2$
221	0.013	203.90	2.62	248	0.014	172.02	2.45
	0.015	178.90	2.18		0.017	150.98	2.02
	0.018	156.89	1.92		0.021	132.11	1.85
	0.021	136.16	1.91		0.025	113.96	1.64
	0.021	137.03	1.72		0.029	95.35	1.37
	0.025	122.65	1.76		0.034	80.44	1.23
	0.025	122.40	1.58		0.056	36.17	0.62
	0.028	107.33	1.37		0.062	28.56	0.49
	0.028	107.72	1.44		0.063	30.39	0.53
	0.032	93.58	1.23		0.063	31.86	0.58
	0.036	80.73	1.11		0.069	23.74	0.41
	0.040	69.69	0.99		0.085	15.75	0.30
	0.045	59.89	0.87		0.092	12.60	0.24
	0.045	57.82	0.94		0.100	9.81	0.19
	0.049	50.71	0.74		0.109	7.64	0.16
	0.050	51.07	0.85		0.117	6.06	0.13
	0.050	51.36	0.78		0.126	4.62	0.10
	0.050	48.93	0.73		0.136	3.53	0.09
	0.055	43.44	0.65		0.136	3.46	0.08
	0.055	41.99	0.65				
	0.060	36.35	0.56				
	0.065	30.01	0.48				
	0.125	5.56	0.11				
	0.133	4.30	0.08				

Table III. Differential pd Elastic Cross Sections.

p_{lab} GeV/c	-t $(GeV/c)^2$	$d\sigma/dt$ $mb/(GeV/c)^2$	$\Delta(d\sigma/dt)$ $mb/(GeV/c)^2$	p_{lab} GeV/c	-t $(GeV/c)^2$	$d\sigma/dt$ $mb/(GeV/c)^2$	$\Delta(d\sigma/dt)$ $mb/(GeV/c)^2$
270	0.014	187.55	2.36	289	0.013	201.66	2.79
	0.017	164.36	1.97		0.015	177.16	2.25
	0.020	145.62	1.87		0.018	155.50	1.97
	0.024	127.26	1.62		0.021	136.18	1.66
	0.028	106.87	1.39		0.071	25.02	0.41
	0.029	99.82	1.30		0.083	17.22	0.29
	0.033	88.50	1.18		0.089	14.32	0.25
	0.034	85.38	1.14		0.096	11.65	0.21
	0.038	72.50	1.00		0.103	9.40	0.18
	0.043	62.12	0.93				
	0.048	51.86	0.78				
	0.049	49.50	0.73				
	0.055	42.93	0.66				
	0.056	39.17	0.60				
	0.061	34.73	0.55				
	0.062	32.70	0.51				
	0.068	26.86	0.43				
	0.127	4.66	0.09				
	0.136	3.67	0.07				

Table III. Differential pd Elastic Cross Sections.

p_{lab} GeV/c	-t $(GeV/c)^2$	$d\sigma/dt$ $mb/(GeV/c)^2$	$\Delta(d\sigma/dt)$ $mb/(GeV/c)^2$	p_{lab} GeV/c	-t $(GeV/c)^2$	$d\sigma/dt$ $mb/(GeV/c)^2$	$\Delta(d\sigma/dt)$ $mb/(GeV/c)^2$
346	0.013	205.34	2.69	384	0.014	187.80	2.37
	0.016	177.06	2.14		0.014	188.72	2.57
	0.018	157.36	1.92		0.017	163.84	1.97
	0.022	136.94	1.74		0.018	149.47	3.81
	0.022	135.86	1.92		0.020	144.13	1.86
	0.025	121.98	1.75		0.024	126.64	1.65
	0.025	121.86	1.62		0.028	106.28	1.43
	0.028	104.66	1.38		0.029	101.11	1.38
	0.028	107.50	1.48		0.033	87.79	1.22
	0.032	91.49	1.23		0.034	84.81	1.18
	0.036	79.09	1.10		0.038	72.53	1.04
	0.041	68.33	0.99		0.043	60.85	0.94
	0.045	58.14	0.88		0.047	53.41	0.78
	0.045	58.00	0.97		0.047	53.56	0.80
	0.050	49.22	0.74		0.048	51.23	0.79
	0.050	50.30	0.79		0.049	49.26	0.75
	0.050	50.50	0.85		0.055	41.88	0.66
	0.050	47.83	0.72		0.056	39.25	0.61
	0.055	42.28	0.65		0.061	34.21	0.55
	0.055	42.02	0.67		0.062	32.20	0.51
	0.060	35.08	0.55		0.068	26.33	0.43
	0.066	29.37	0.48		0.103	9.03	0.38
	0.126	5.25	0.11		0.128	4.66	0.09
	0.133	3.99	0.08		0.137	3.47	0.07

Table IV. Total pd Elastic Cross Sections.

p_{lab} (GeV/c)	σ_{el} (mb)	σ_{el}/σ_{tot}
49	7.45 ± 0.04	0.1018 ± 0.0003
72	7.25 ± 0.05	0.0992 ± 0.0004
148	7.07 ± 0.04	0.0963 ± 0.0003
174	7.09 ± 0.05	0.0962 ± 0.0005
221	7.13 ± 0.05	0.0964 ± 0.0004
248	7.11 ± 0.04	0.0958 ± 0.0004
270	7.09 ± 0.05	0.0953 ± 0.0004
289	7.13 ± 0.05	0.0957 ± 0.0005
346	7.23 ± 0.05	0.0964 ± 0.0004
384	7.23 ± 0.05	0.0961 ± 0.0004

Overall energy independent systematic uncertainty not included.

Table V. Glauber Approach - Sum of Exponentials Form Factor $b_{pn} = b_0 + b_1 \ln s_{pp}$.

Neutron Slope		Form Factor					χ^2
b_0 $(GeV/c)^{-2}$	b_1 $(GeV/c)^{-2}$	A_1	A_2	B_1 $(GeV/c)^{-2}$	B_2 $(GeV/c)^{-2}$	B_3 $(GeV/c)^{-2}$	
8.23	0.556	0.352 ± 0.003	0.571 ± 0.010	141.5	26.1	15.5	288
Fixed	Fixed			Fixed	Fixed	Fixed	
8.23	0.556	0.34	0.58	137.7 ± 1.3	29.5 ± 0.1	2.33 ± 0.33	289
Fixed	Fixed	Fixed	Fixed				
5.57 ± 0.54	1.15 ± 0.10	0.34	0.58	141.5	26.1	15.5	269
		Fixed	Fixed	Fixed	Fixed	Fixed	
5.84 ± 0.49	1.16 ± 0.09	0.354 ± 0.003	0.517 ± 0.011	141.5	26.1	15.5	240
				Fixed	Fixed	Fixed	

FIGURE CAPTIONS

Fig. 1. Schematic layout of the experiment. The deuterium gas jet fires vertically (perpendicular to the figure). The detectors are on a movable carriage and at a constant distance of 2.5 meters from the beam-jet intersection point.

Fig. 2. Typical operating conditions. The jet is pulsed three times, at nominal incident momenta of 50, 175, and 250 GeV/c.

Fig. 3. Electronics schematic.

Fig. 4. Scatter plot of T_F vs T_B, the energies deposited in the front and back detector elements. In this example the front detector was 0.2-mm thick, the back detector 2-mm thick.

Fig. 5. Mass of particles registered in a detector stack.

Fig. 6. Kinetic energy distribution of deuterons at 50 and 250 GeV/c incident momentum.

Fig. 7. Differential cross sections at 49 GeV/c and 384 GeV/c.

Fig. 8. b, and c, as a function of p_{lab} obtained from fits to the Bethe interference formula. Δ from Ref. 1. • this experiment. The cross-hatched regions are a fit to our experiment only.

Fig. 9. σ_{el}/σ_{tot} (pd) as a function of incident momentum. Δ are from Ref. 17. • are from this experiment. The dashed curve is described in the text.

Fig. 10. IG, the Glauber integral as a function of p_{lab}.

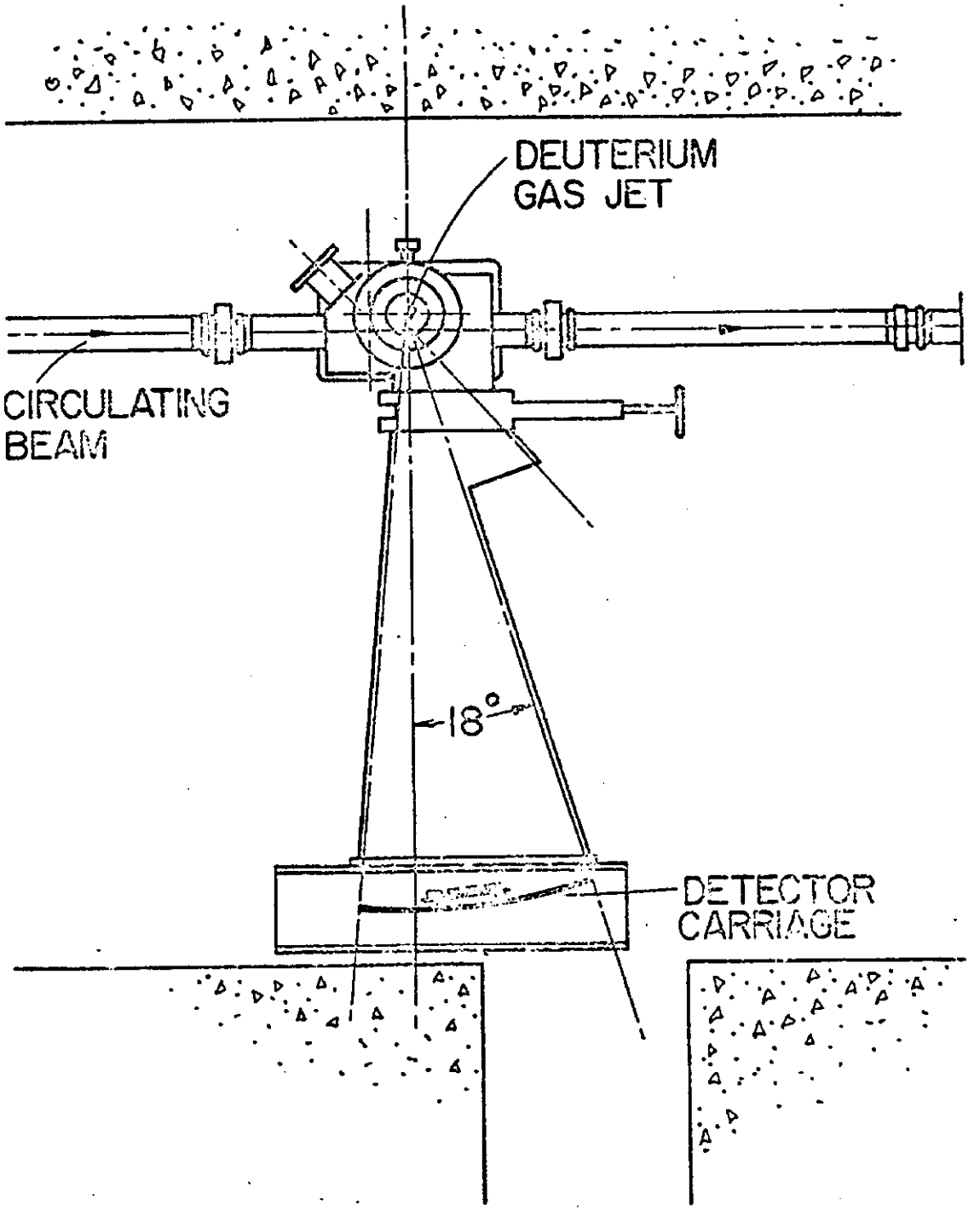

Fig. 1

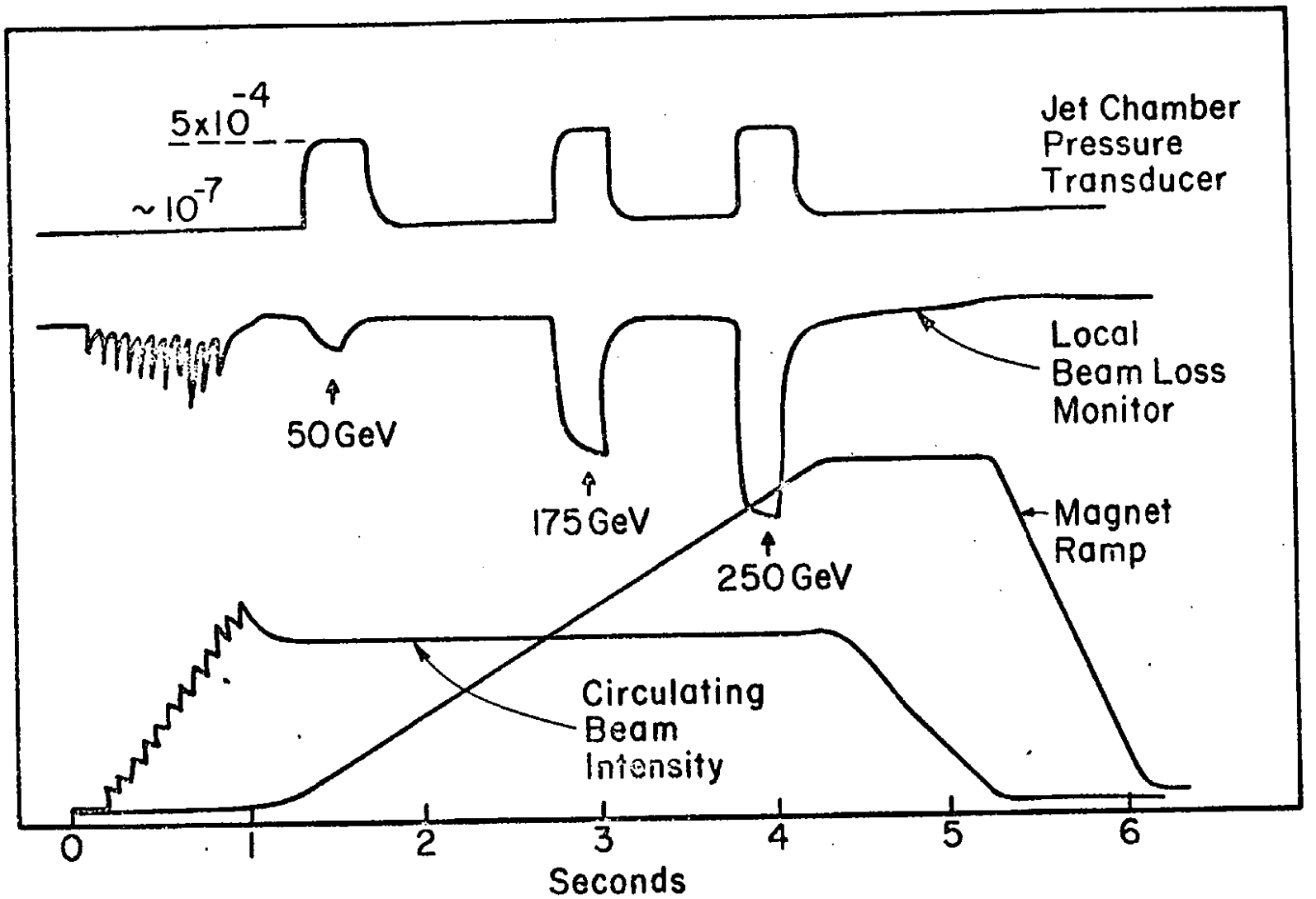
5×10^{-4}
$\sim 10^{-7}$
Jet Chamber
Pressure
Transducer
50 GeV
175 GeV
250 GeV
Local
Beam Loss
Monitor
Magnet
Ramp
Circulating
Beam
Intensity
0
1
2
3
4
5
6
Seconds

Fig. 2

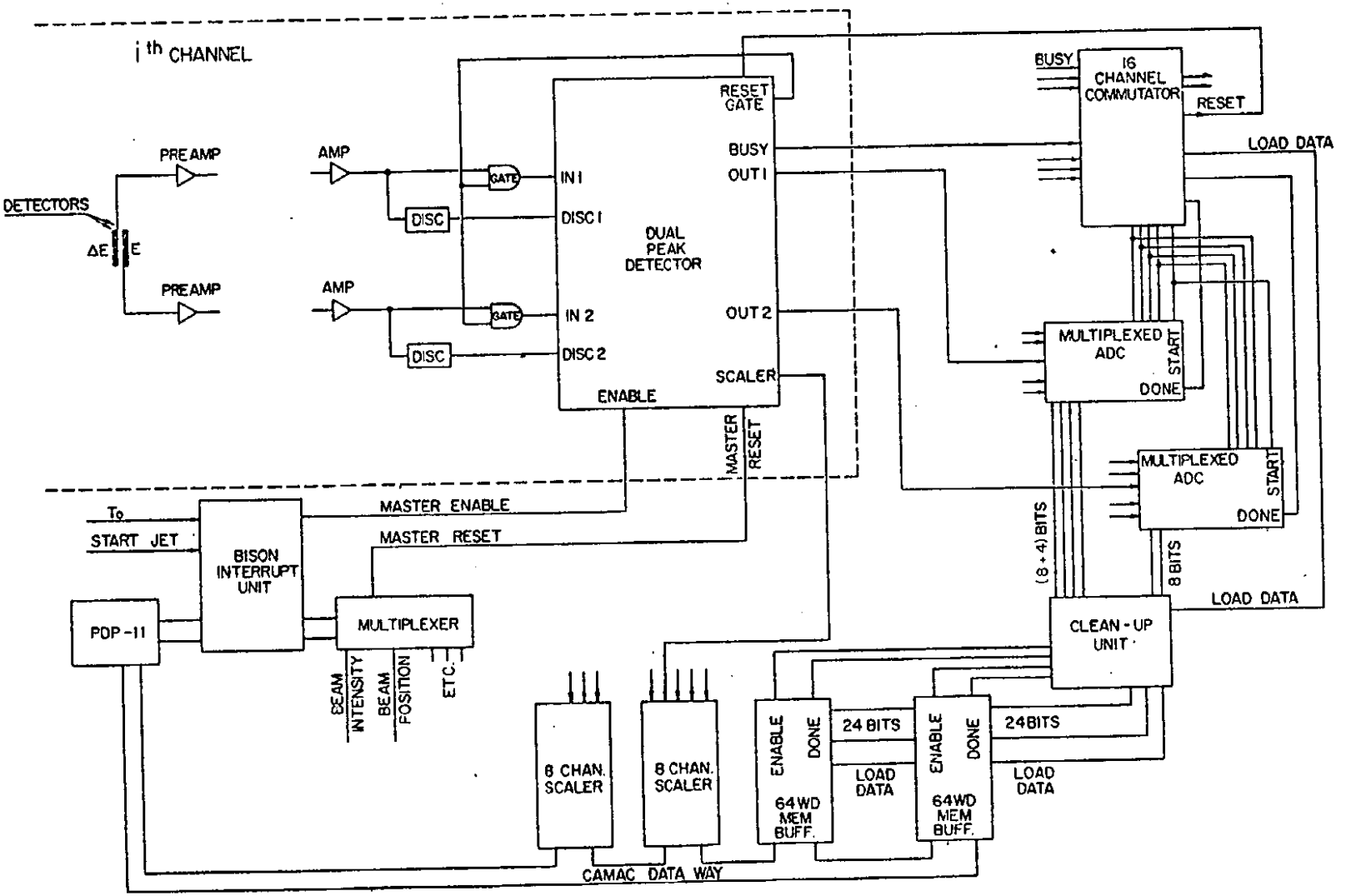
i th CHANNEL
PREAMP
DETECTORS
ΔE
E
PREAMP
AMP
DISC
GATE
IN 1
DISC 1
AMP
DISC
GATE
IN 2
DISC 2
DUAL PEAK DETECTOR
RESET GATE
BUSY
OUT 1
OUT 2
SCALER
ENABLE
MASTER RESET
BUSY
16 CHANNEL COMMUTATOR
RESET
LOAD DATA
MULTIPLEXED ADC
START
DONE
MULTIPLEXED ADC
START
DONE
(8+4) BITS
8 BITS
LOAD DATA
CLEAN-UP UNIT
To START JET
BISON INTERRUPT UNIT
MASTER ENABLE
MASTER RESET
PDP-11
MULTIPLEXER
BEAM INTENSITY
BEAM POSITION
ETC.
8 CHAN. SCALER
8 CHAN. SCALER
ENABLE
DONE
64 WD MEM BUFF.
24 BITS
LOAD DATA
ENABLE
DONE
64 WD MEM BUFF.
24 BITS
LOAD DATA
CAMAC DATA WAY

Fig. 3

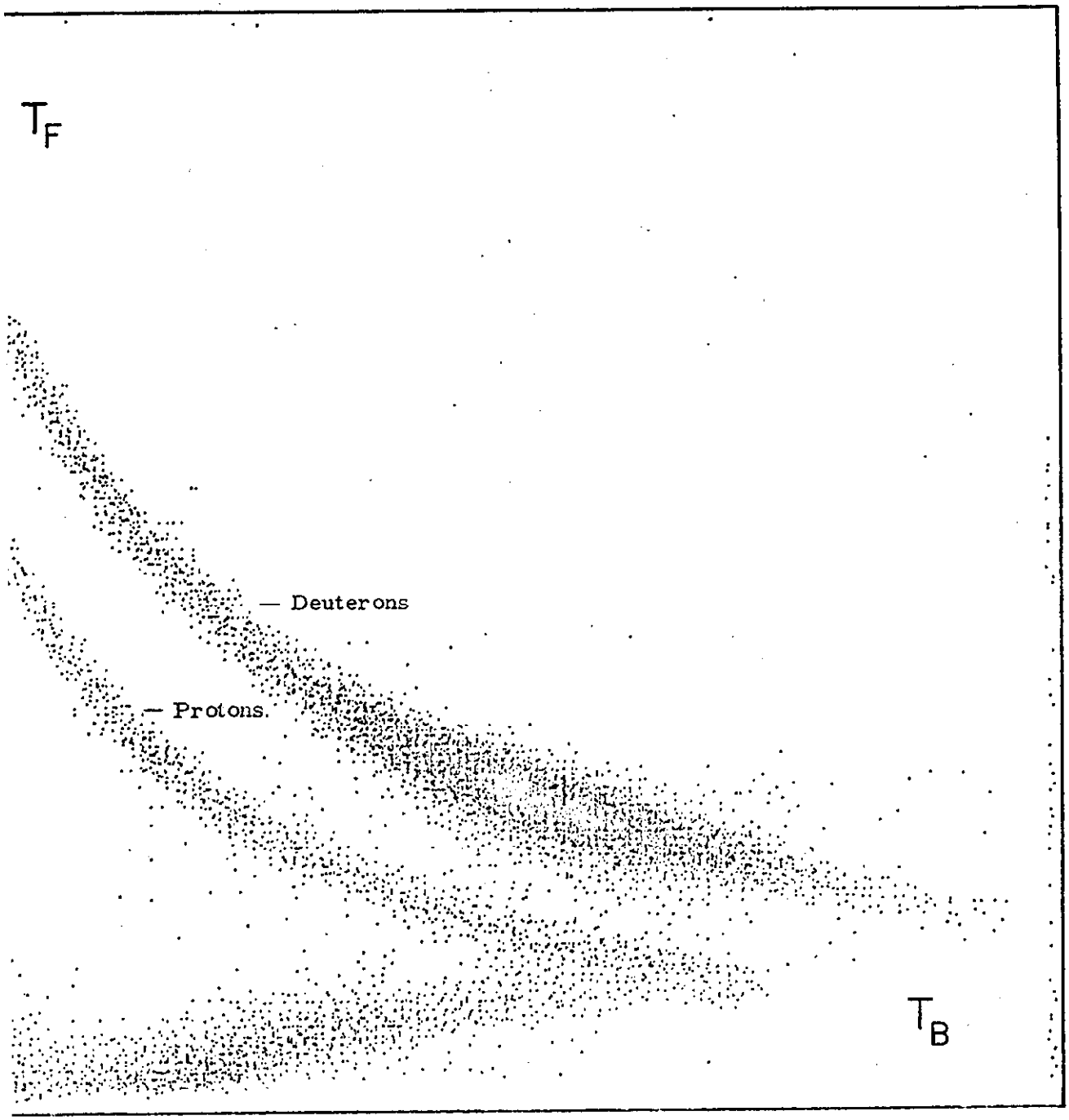

Fig. 4

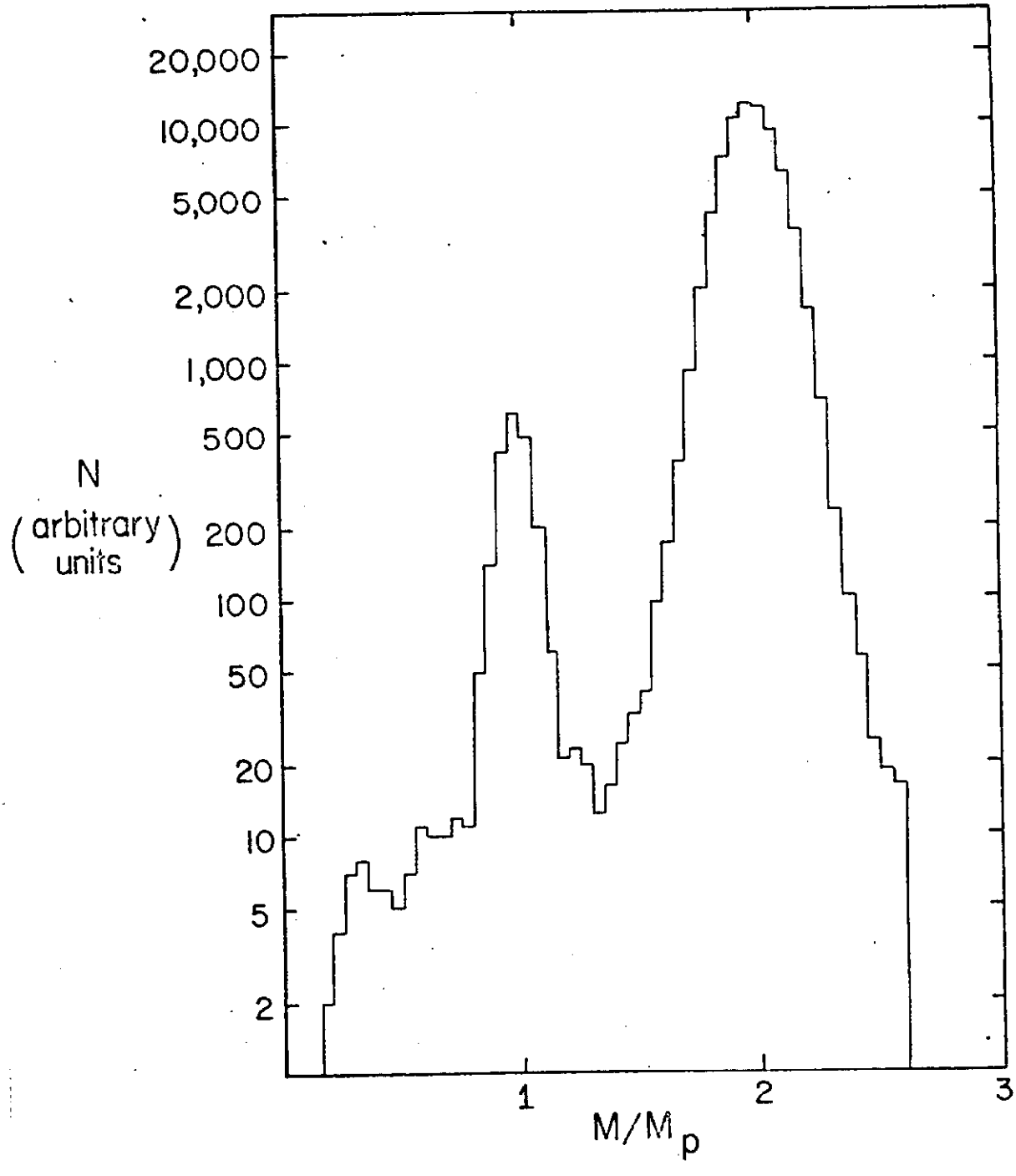
20,000
10,000
5,000
2,000
1,000
500
200
100
50
20
10
5
2
N
(arbitrary units)
1
2
3
M/M p

Fig. 5

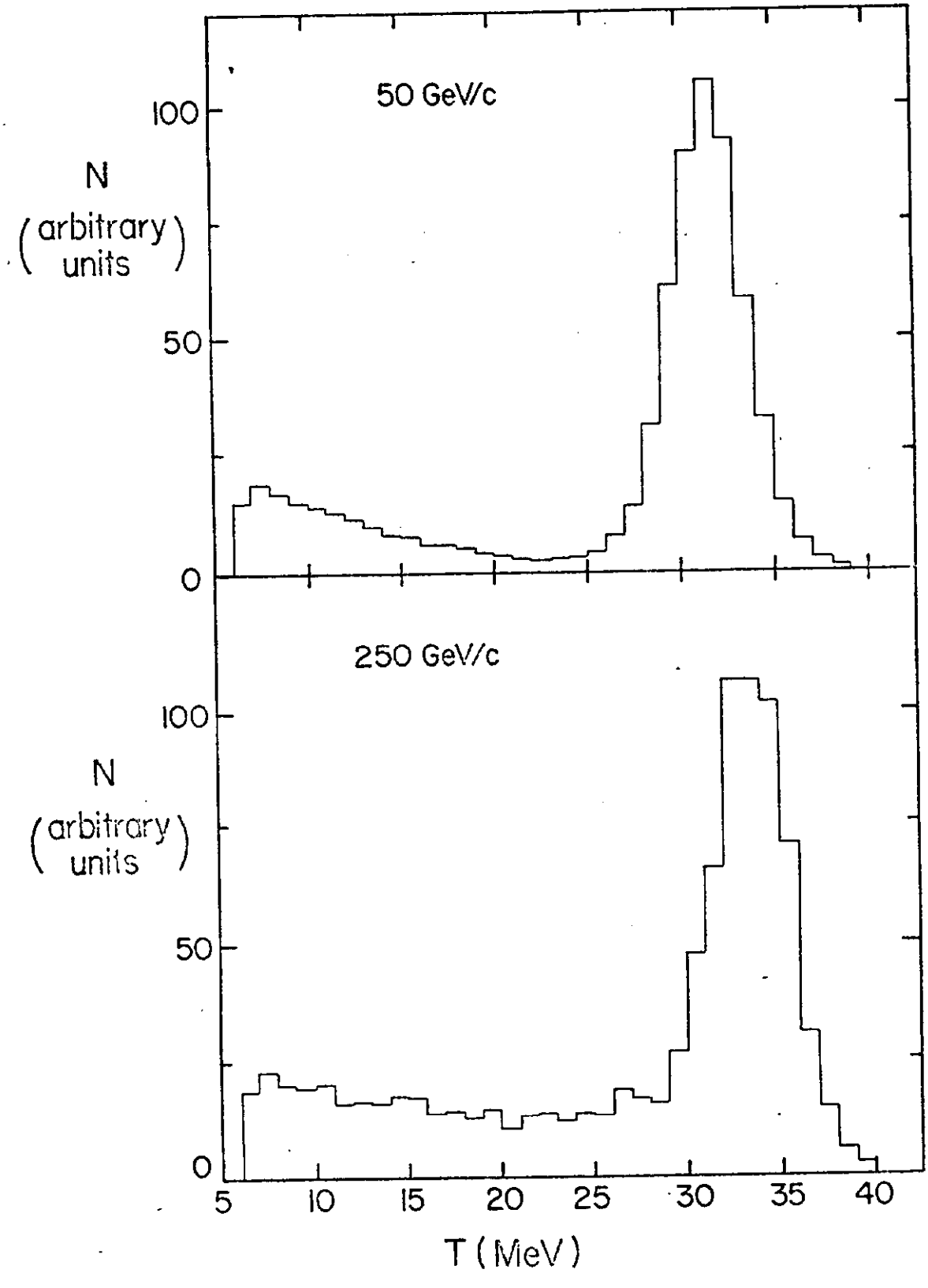
50 GeV/c
100
N
(arbitrary units)
50
0
250 GeV/c
100
N
(arbitrary units)
50
0
5
10
15
20
25
30
35
40
T (MeV)

Fig. 6

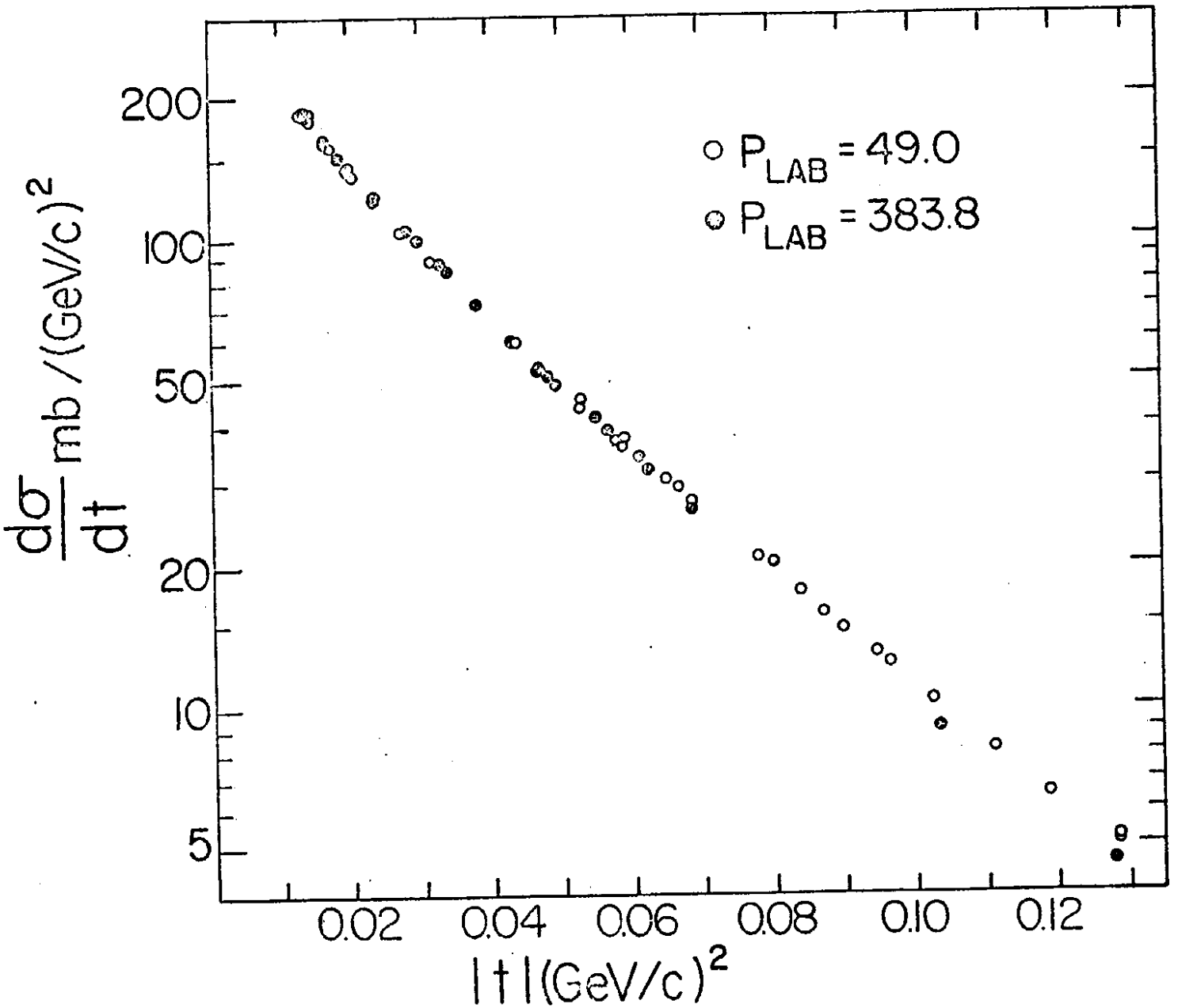
200
100
50
20
10
5
0.02
0.04
0.06
0.08
0.10
0.12
$\frac{d\sigma}{dt}$ mb/(GeV/c)^2
|t| (GeV/c)^2
P_{LAB} = 49.0
P_{LAB} = 383.8

Fig. 7

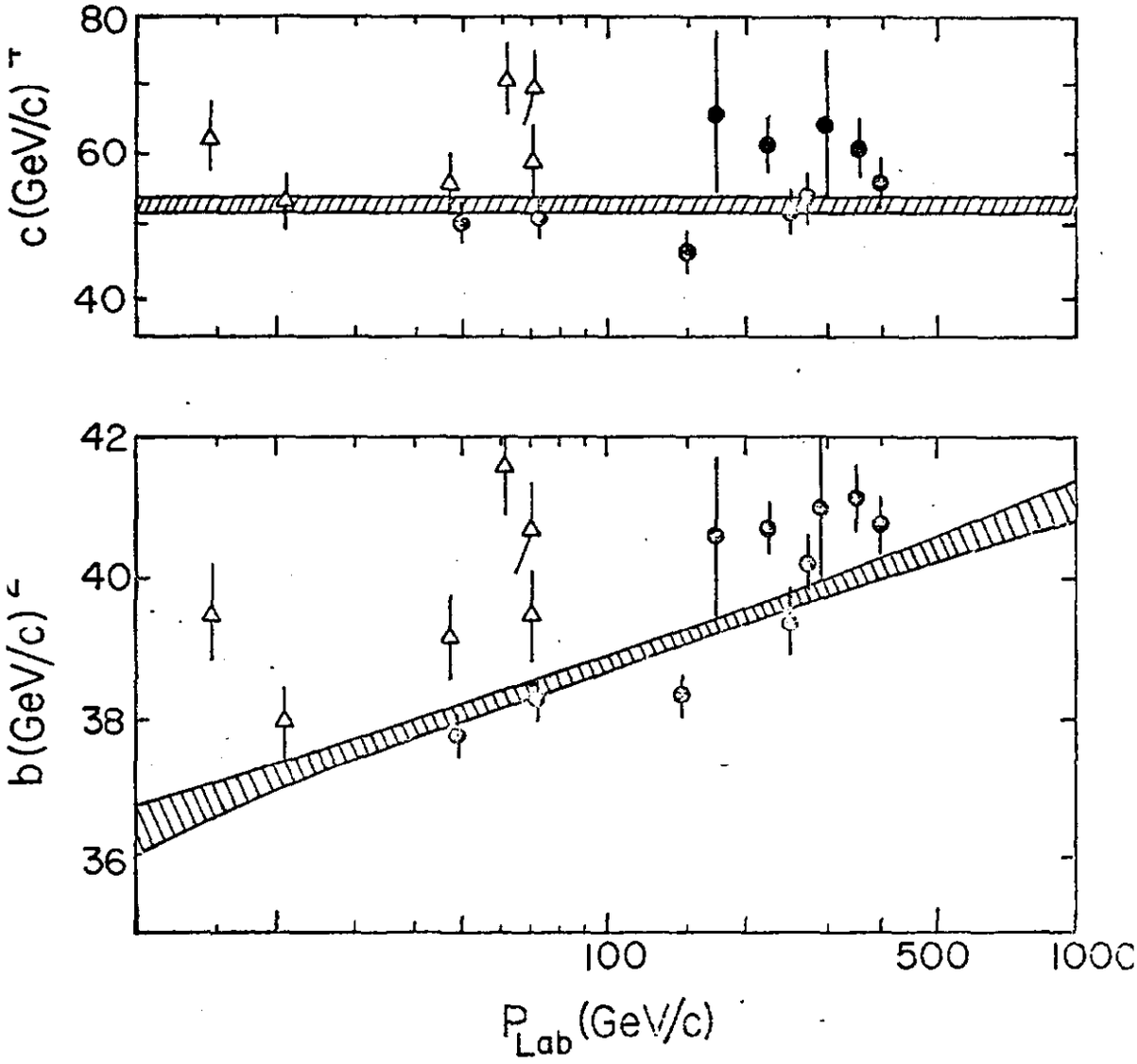

Fig. 8

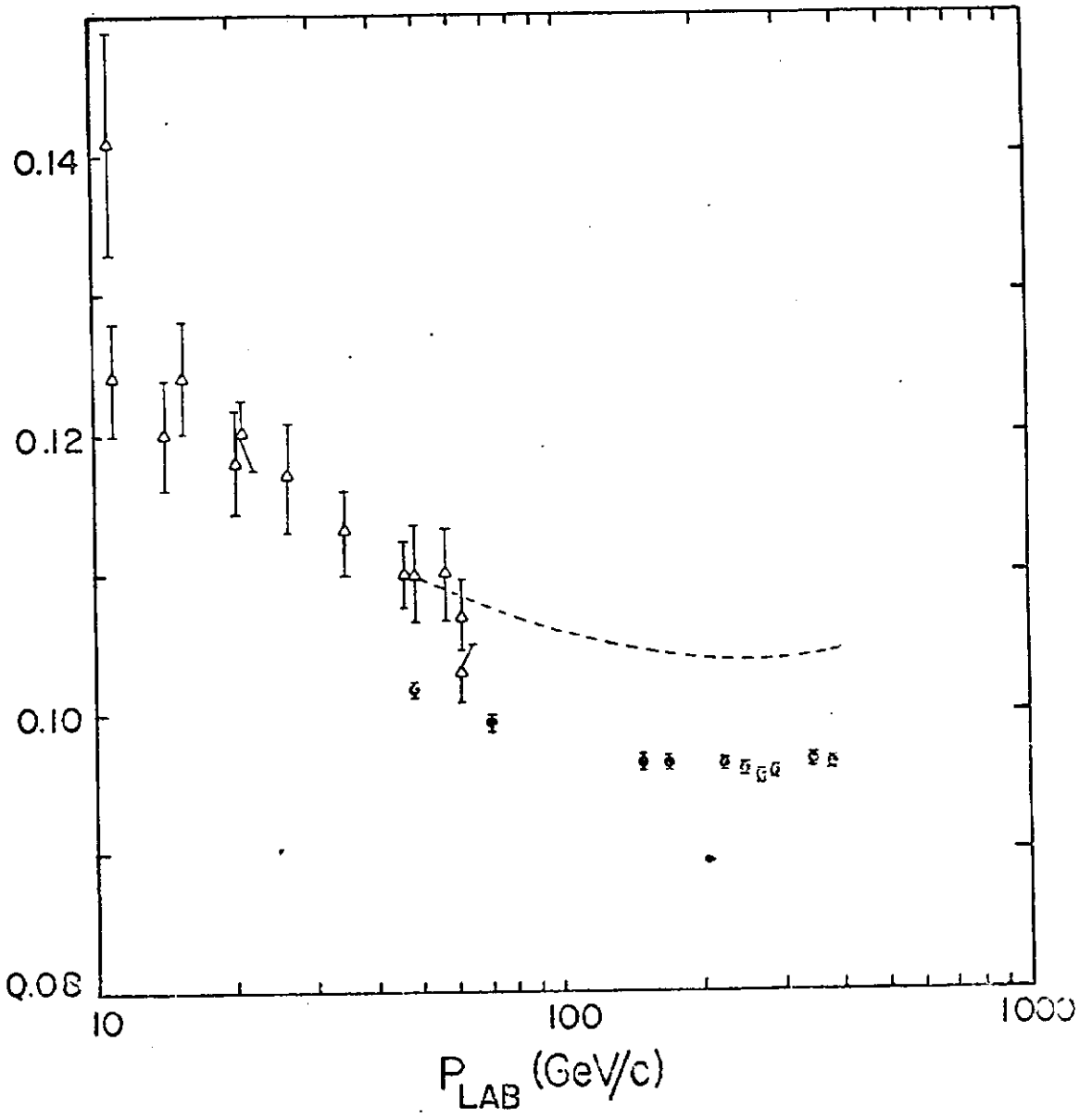

Fig. 9

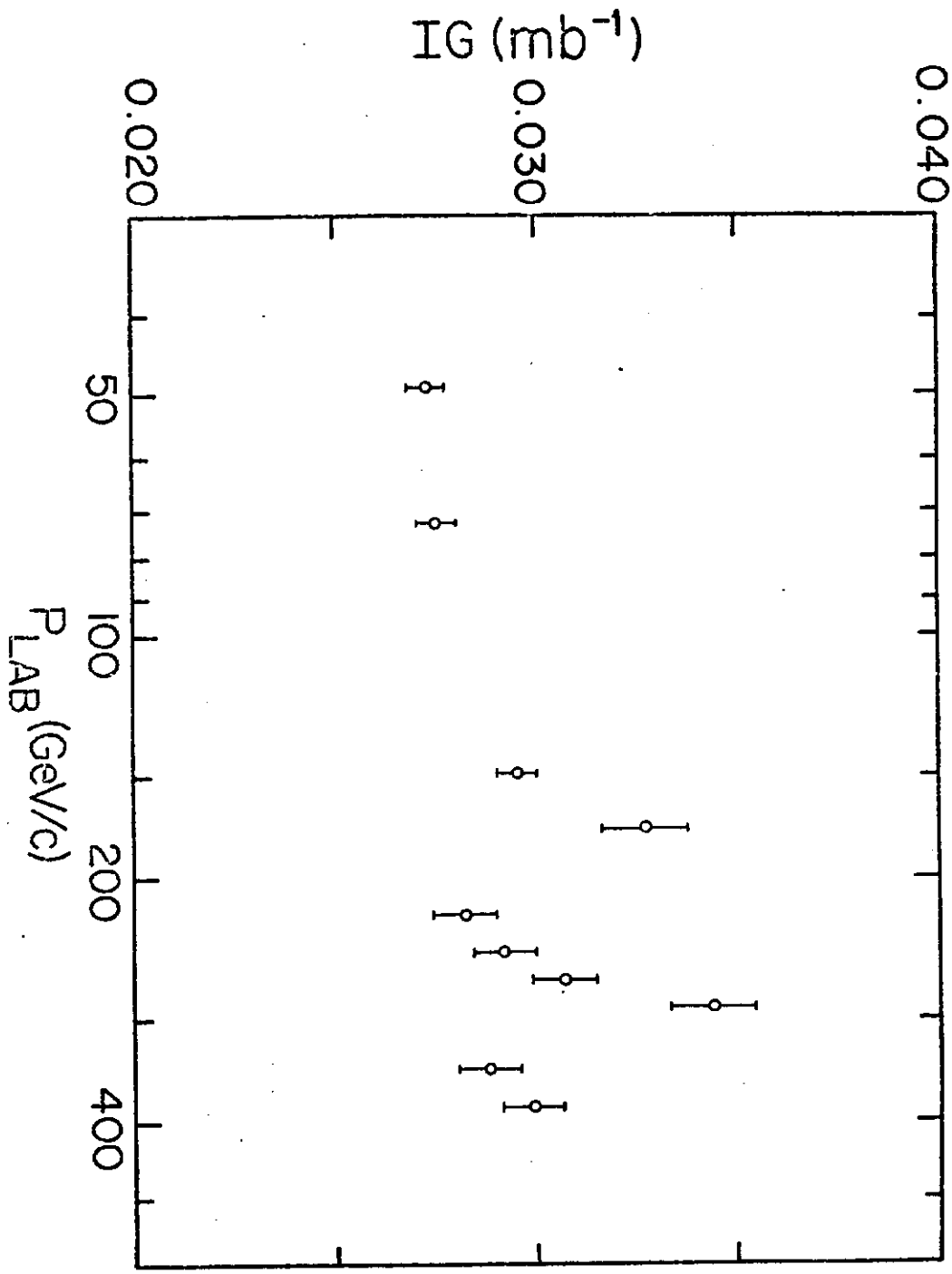

Fig. 10